Time-Domain Equivalent Model for Harmonic Simulations of Wind and Photovoltaic Plants

Alex Reis[1], Anésio de L. F. Filho[1], Pedro H. F. Moraes[2]

[1]University of Brasília (UnB), Brasília, Brazil
[2]Federal Institute of Goiás (IFG), Valparaíso, Brazil
alexreis@unb.br, leles@ene.unb.br,
pedro.moraes@ifg.edu.br

Juliana P. de Lima[3], Mohamad S. I. Neto[3], Vinícius dos Passos[3]

[3]Copel Geração e Transmissão S.A., Curitiba, Brazil
[juliana.lima, mohamad.neto, vinicius.passos]@copel.com

Abstract—**Equivalent models of wind power plants or photovoltaic systems reduce the computational burden relative to detailed models (DMs) during power quality studies. However, existing time-domain equivalent models are ineffective for predicting harmonic currents because they do not consider switching behavior from power converters. This paper proposes a novel time-domain equivalent model, the aggregated harmonic model (AHM), to perform harmonic current prediction in large plants. The AHM uses the National Renewable Energy Laboratory method to equalize the collector system and applies the superposition principle to include the dead time and switching effects. Simulations were executed using the DM and AHM of actual plants. Field measurements were performed to validate the AHM. The results show that the proposed model produced well-matched curves for current waveforms, frequency responses, and harmonic spectra. Consequently, this model is an accurate tool for transmission system operators.**

Index Terms--**Equivalent model, harmonic distortion, power quality, renewable energy, time-domain modeling.**

I. INTRODUCTION

With the increasing use of grid-connected wind power plants (WPPs) and photovoltaic (PV) systems, electric grids have faced technical challenges in the areas of transient stability, small-signal stability, frequency stability, and power quality [1]. Consequently, it is necessary to analyze the penetration impacts of renewable energy sources (RESs) on the harmonic profile of large-scale power systems [2]. However, large plants typically have several wind turbines (WTs) or PV inverters, which increases the complexity of modeling these systems. This makes it difficult to fully simulate the entire facility owing to the model size and computational burden. Therefore, the need for comprehensive harmonic analyses requires the development of equivalent new models for large RES-based plants that are accurate and computationally efficient [3].

Li et al. [3] outlined a three-step approach for creating effective equivalent models of WPPs or PV plants. Firstly, an individual model for each WT must be developed. Next, these individual models are aggregated into a single unit or a small number of units. Finally, the clustering of WTs should accurately reflect the equivalence of the collector system of the WPP, as detailed in [4].

Regarding the modeling of individual grid-connected inverters, the authors in [5]-[7] discuss various methodologies, including frequency-domain impedance models (IMs) and time-domain detailed or simplified models (DMs and SMs, respectively). DMs typically require numerous parameters as they rely on differential equations to simulate real-world equipment. This condition imposes a significant computational burden, rendering DMs impractical for simulating large PV plants or WPPs. In contrast, SMs are better suited for large-scale installations due to their operation within a reduced bandwidth. In [6], the authors present an SM employing a controllable voltage source to represent grid-connected inverters. A switching emulator is included to consider the harmonic content in current and voltage waveforms. In [5], a harmonic average model is proposed to predict the harmonic currents of individual WTs and PV units. This model incorporates dead time and switching effects to reproduce baseband, sideband, and carrier harmonic components. Both papers emphasize including switching effects to enhance SMs for system-level harmonic studies.

Concerning the clustering of WTs or PV inverters, as discussed in [8], the equivalent models can be categorized into multi-machine and single-machine topologies. In the multi-machine topology, the entire plant is reduced to a few equivalent units through the application of coherency-based equivalence. This method involves aggregating generators with similar operating conditions into one equivalent unit. While this approach offers high accuracy, it relies on complex procedures for detecting logical classification indexes, limiting its practical applications [9]. Conversely, the single-machine topology does not involve combining WTs in small groups. Instead, it aggregates the entire WPP into one equivalent unit [10], thereby reducing the computational burden. However, single-machine equivalent models, though computationally efficient, often neglect fast-scale dynamics [8], leading to potential errors in harmonic emission levels when compared with DMs or actual plants. To address this limitation, there is

potential for improvement in high-frequency responses by integrating commutation effects into the conversion system of a single-machine model.

Some studies in the literature proposed improvements for single-machine equivalent models, approximating the simulated results to field measurements. These proposals rely on fuzzy logic [11], dynamic weighted aggregation [12], self-organizing map neural network [13], multi-objective optimization [14], and calibrating the power recovery [9]. Although these studies developed robust models, their approaches are difficult to deploy, as they rely on extensive routines or optimization calculations. In addition, they did not consider harmonic emissions from the commutation process in their models.

To overcome these limitations, the authors in [15], [16] proposed equivalent harmonic models in the frequency domain. In [15], Wang, Buchhagen, and Sun presented four frequency-domain impedance models that included harmonic content from WPPs. These impedance models were developed in the presence of coupling effects in the individual turbine responses. Cao et al. [16] presented a new sum-type impedance model for grid-connected inverters based on the global admittance from the point of connection (PoC). This approach helped the analysis of system stability and revealed the influence of each inverter on the system stability. It also had a low computational burden. However, frequency-domain impedance models suffer from some drawbacks: i) harmonic currents and inverter impedances, which can be difficult to obtain, are required as input data; ii) detecting inconsistencies is challenging; iii) the results reflect snapshot scenarios because they are valid only for specific load conditions; and iv) harmonic impedances are obtained using the admittance matrix; therefore, only passive components are considered [17]. Frequency-domain models ignore nonlinear behaviors, whereas time-domain models rely on differential equations that approximate computer simulations to real-world operations. Therefore, researchers and scholars employ time-domain models or field measurements to validate frequency-domain models [18].

Equivalent models used for harmonic assessments need to i) reproduce the harmonic currents affected by the converter switching devices and ii) represent the interactions between the model and the grid, such as resonance conditions [18]. According to Pourbeik et al. [19], there is a significant demand for time-domain equivalent models that are accurate, easy to implement, and operate as generic and simplified structures without detailed parameters or a heavy computational burden. In the literature, existing time-domain equivalent models neglect fast-scale dynamics, such as the baseband, sideband, and carrier harmonic components. Thus, these models are ineffective for predicting harmonic currents [20]. In addition, these existing equivalent models use complex procedures for approximating the simulated results to field measurements [21].

This paper introduces a time-domain equivalent model, referred to as the Aggregated Harmonic Model (AHM),

designed to predict the harmonic currents of WPPs and PV plants. The AHM combines grid-connected inverters into an equivalent model and employs the superposition principle to incorporate dead time and switching effects, aiming to accurately reproduce baseband, sideband, and carrier harmonics. To assess its performance, the AHM is compared with DMs applied to a 28.2-MW WPP and a 32MW PV plant. Additionally, field measurements are conducted on another WPP to validate the AHM's harmonic estimation capability. This comparative analysis and validation process contribute to evaluating the effectiveness and reliability of the AHM in predicting harmonic currents in renewable energy systems.

The proposed methodology uses the National Renewable Energy Laboratory (NREL) method [4] to develop model equivalences for the generators, transformers, and collector systems of a power plant. As a result, a single-machine model that represents the entire facility is developed.

The main contributions of this paper are as follows:

- We propose an aggregated harmonic time-domain model, based on a single-machine equivalent model, to predict the harmonic currents of WPPs and PV plants. Although this AHM is developed with the actual parameters of three specific Brazilian plants, it can represent other Renewable Energy Sources (RESs) by adapting the model parameters to the specifications of the relevant generation system.

- This expanded method includes the harmonic behavior from power converters in the time-domain equivalent models. This strategy seeks to enhance the accuracy of existing time-domain single-machine models while preserving a simple model format. Two effects were considered: dead time and switching patterns.

The remainder of this paper is organized as follows: Section II introduces the NREL method and outlines the proposed AHM. Section III discusses the plants simulated in this study and presents the results of comparing the AHM with DMs and with field measurements. Finally, conclusions are provided in Section IV.

II. THE NREL METHOD AND THE PROPOSED AGGREGATED HARMONIC MODEL

A. NREL Single-Machine Equivalent Model

Fig. 1 presents a single-line diagram of a generic power plant (Fig. 1a) connected to a transmission system through a collector substation and its respective equivalent single-machine model (Fig. 1b). An equivalent model is developed according to the NREL method [4].
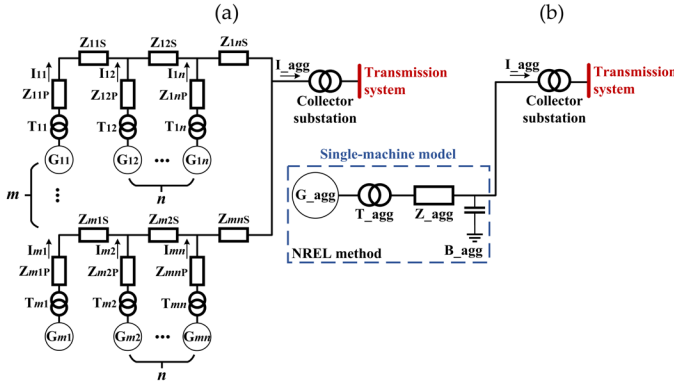
Figure 1. Single-line diagram of (a) a generic power plant and its respective (b) equivalent single-machine model.

In Fig. 1a, m and n represent the matrix indices of the entire plant. Gmn, Tmn, $ZmnP$, $ZmnS$, Imn, and I_agg represent the generators, transformers, parallel impedances, series impedances, individual injected currents, and aggregated injected current, respectively. In Fig. 1b, G_agg, T_agg, Z_agg, and B_agg represent the aggregated generators, transformers, impedances, and susceptances, respectively.

According to the NREL method [4], $ZmnP$ can be disregarded because its values are much smaller than those of $ZmnS$. The NREL method is defined as follows:

$$G\_agg = \sum_{i=1}^{q_{total}} G_i \tag{1}$$

$$T\_agg = Z_{T_{11}}/q_{total} \tag{2}$$

$$Z\_agg = \frac{\sum_{k=1}^{n_{line \, and \, cable}} Z_{kS} \cdot q_{upstream_k}^2}{q_{total}^2} \tag{3}$$

$$B\_agg = \sum_{k=1}^{n_{line \, and \, cable}} B_k \tag{4}$$

where q_{total} and $q_{upstream}$ denote the number of WTs in the plant and the WTs located upstream of a given line or cable, respectively. The terms G_i, Z_{T11}, Z_{kS} and B_k represent the rated power of a generator in the plant, impedance of a transformer in the plant, series impedances, and shunt susceptances of each line and cable, respectively.

B. Proposed Aggregated Harmonic Model

Fig. 2 shows the proposed AHM based on the single-machine equivalent model presented in Fig. 1.

Fig. 2 shows that the T_agg, Z_agg, and B_agg are the same as described in (2), (3), and (4), respectively. However, we propose a novel strategy to aggregate generators in the AHM (G_ahm). The G_ahm uses a single-machine average model that replaces the RES with a controllable current source (I_ahm). This current source depends on the total aggregated input power G_agg (Fig. 1) and the DC-link voltage (V_{DC}). The inverter is replaced by an average model, which has the

DC side represented by a current source (I_{conv}) and the AC side reproduced by three controllable voltage sources ($v_{a,b,c}^{AHM}$).
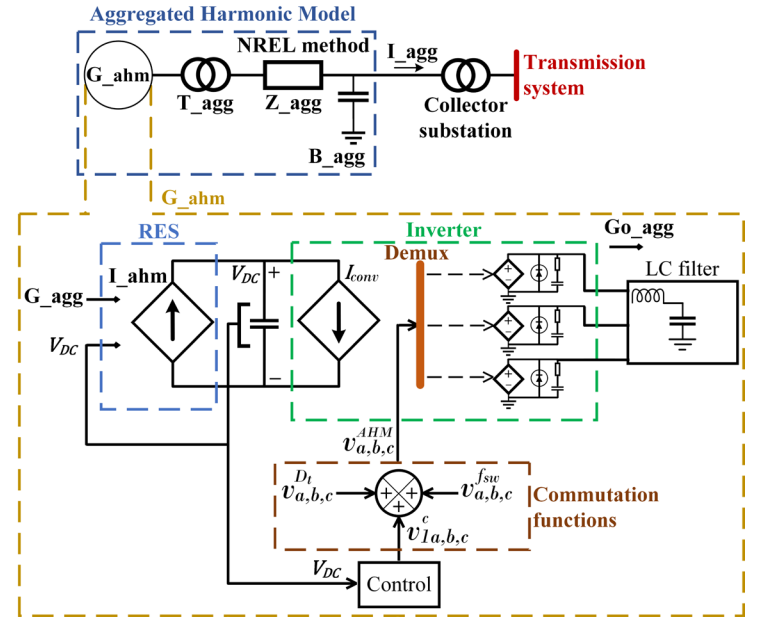

Figure 2. Single-line diagram of (a) a generic power plant and its respective (b) equivalent single-machine model.

In contrast to existing single-machine models [3], [4], which neglect fast-scale dynamics, we applied the superposition principle to add the commutation functions of dead time ($v_{a,b,c}^{Dt}$) and switching effects ($v_{a,b,c}^{fsw}$) to the fundamental components ($v_{a,b,c}^{c}$), keeping control loops unchanged. Finally, an inductor–capacitor (LC) filter is included to mitigate the high-frequency components.

The current sources I_ahm and I_{conv} are controlled by:

$$I\_ahm = G\_agg/V_{DC} \tag{5}$$

$$I_{conv} = Go\_agg/V_{DC} \tag{6}$$

where G_agg and Go_agg represent the input and output powers of the aggregated generators, respectively.

According to [22], we can represent the dead time of the inverter as three-square waves that depend on the DC-link voltage, dead time (D_t), switching period (T_{sw}), and output currents ($i_{2a,b,c}$). The amplitudes of these waves are defined as

$$\begin{bmatrix} v_a^{D_t} \\ v_b^{D_t} \\ v_c^{D_t} \end{bmatrix} = -\frac{V_{DC} \cdot D_t}{T_{sw}} \begin{bmatrix} \text{sign}(i_{2a}) \\ \text{sign}(i_{2b}) \\ \text{sign}(i_{2c}) \end{bmatrix} \tag{7}$$

In addition, we incorporate the switching effects into the fundamental voltages, defining these three-phase voltages:

$$\begin{bmatrix} v_a^{f_{sw}} \\ v_b^{f_{sw}} \\ v_c^{f_{sw}} \end{bmatrix} = \begin{bmatrix} \dfrac{2.V_{DC}}{\pi} \sum\limits_{y=1}^{\infty} \sum\limits_{z=-\infty}^{\infty} \dfrac{1}{y}.J_z\left(y.\dfrac{\pi}{2}.M\right).A.U_a \\[2ex] \dfrac{2.V_{DC}}{\pi} \sum\limits_{y=1}^{\infty} \sum\limits_{z=-\infty}^{\infty} \dfrac{1}{y}.J_z\left(y.\dfrac{\pi}{2}.M\right).A.U_b \\[2ex] \dfrac{2.V_{DC}}{\pi} \sum\limits_{y=1}^{\infty} \sum\limits_{z=-\infty}^{\infty} \dfrac{1}{y}.J_z\left(y.\dfrac{\pi}{2}.M\right).A.U_c \end{bmatrix} \quad (8)$$

considering,

$$A = \sin([y+z].\,\pi/2) \quad (9)$$

$$U_a = \cos(y.\omega_{sw}.t+z.\omega_g.t) \quad (10)$$

$$U_b = \cos(y.\omega_{sw}.t+z.[\omega_g.t-2\pi/3]) \quad (11)$$

$$U_c = \cos(y.\omega_{sw}.t+z.[\omega_g.t+2\pi/3]) \quad (12)$$

where y and z represent the carrier and sideband components, respectively. J, M, ω_{sw}, and ω_g denote the Bessel function of the first kind, the modulation index of the inverter, switching frequency, and grid frequency, respectively. Equation (8) reproduces a sampled modulation strategy known as sinusoidal pulse-width modulation (SPWM) with a triangle-based function, which operates as the carrier wave [23].

By analyzing (7) - (12), we can observe that the proposed AHM is directly affected by M. This variable impacts the fundamental voltages, DC-link voltages, and commutation functions. For this reason, the AHM can thus represent the baseband, sideband, and carrier components for distinct values of M. Additionally, by inserting the commutation functions externally, this strategy ensures the generality of the proposed method because no modifications in the control loops are required.

C. Control Loops of the Aggregated Harmonic Model

Fig. 3 presents the pulse-width modulation (PWM) model with a V_{DC} control selected for this study. It helps achieve an accurate representation of the inverter operation because it introduces ripples in the DC-link voltage.
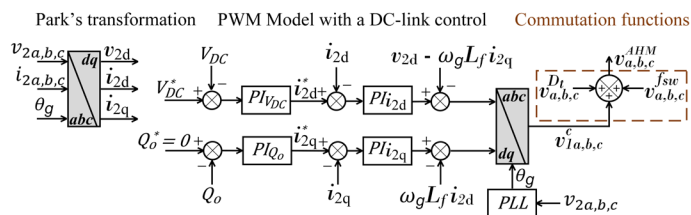

Figure 3. Block diagram of the PWM model with DC-link control.

In Fig. 3, $v_{2a,b,c}$ and $i_{2a,b,c}$ (where a, b, and c represent the phases) denote the voltages and currents after the filter, respectively; $v_{2d,q}$ and $i_{2d,q}$ denote the voltages and currents referred to the dq-components; L_f, R_f, θ_g, and ω_g represent the filter inductance, filter resistance, grid angle, and grid

frequency, respectively. The $v_{c1a,b,c}$ represents the fundamental voltages of the commutation functions.

Fig. 3 shows that the PWM model with a V_{DC} control has an outer loop that controls the DC-link voltage and another outer loop that adjusts the reactive power. In most cases, the power factor is unity, which implies that $Q_0^* = 0$. Further, the control has two inner loops: one for the direct (d) current and the other for the quadrature (q) current. A phase-locked loop (PLL) synchronizes the inverter by estimating θ_g and ω_g. An inverse Park transformation provides instantaneous voltages $v_{c1a,b,c}$. This control employs a synchronous reference frame and proportional-integral (PI) controllers PI_{VDC}, PI_{Qo}, PI_{i2d}, and PI_{i2q}. Although we selected the PI-control topology presented in Fig. 3, different control schemes can be used to implement the AHM, for example, PI, proportional–resonant, hybrid loops, and repetitive controllers.

For situations in which grid-connected inverters have different structural or operational characteristics, clustering techniques [3] remain an alternative to represent the equivalent harmonic emissions of the generation system. In this case, each inverter is grouped with similar units, enabling the development of an equivalent representation for each group.

III. CASE STUDIES

A. Methodology

The methodology employed to evaluate the performance of the AHM is based on three case studies conducted on real-world WPPs and PV plants. The assessment of the AHM involves its ability to generate current waveforms affected by the nonlinear behavior of power converters, its capability to replicate the harmonic impedance of a power plant, its accuracy in predicting harmonic spectra, and its computational efforts. The case studies are described as follows:

- *Case 1: Investigation of harmonic emissions from a 28.2-MW WPP situated in the northeast region of Brazil.* Field measurements were conducted at the medium-voltage side of a WT's coupling transformer to validate a DM of an individual 2.35-MW WT. Subsequently, this DM was extrapolated to simulate the entire wind power plant DM_{WPP}. The total harmonic current injected by the DM_{WPP} was compared with the corresponding AHM_{WPP}.

- *Case 2: Analysis of harmonic emissions from a 32-MW PV plant located in the southeast region of Brazil.* Similar to Case 1, field measurements were taken at the medium-voltage side of a coupling transformer to validate a DM of a 4-MW PV inverter. Based on this individual model, the entire PV plant (DM_{PV}) was simulated, and the harmonic current injected into the transmission system was compared with simulations of the corresponding AHM_{PV}.

- *Case 3: Examination of another WPP with an installed capacity of 27.3 MW in the northeast region of Brazil.* Field measurements were conducted at the point of connection of the power plant. The measured harmonic

currents were compared with simulations from the corresponding AHM$_{WPP2}$.

All case studies were simulated using MATLAB. Based on equations (1)-(4), an AHM was developed for each case, resulting in the parameters presented in Table 1. For consistency, the grid-connected inverters in each case study were assumed to have the same control parameters. A comprehensive list of system parameters is available in [21].

Model	G_agg (MW)	T_agg (pu)	Z_agg (pu)	B_agg (pu)
AHM$_{WPP}$	28.2	0.062/12	0.0229+0.0505i	2.1545
AHM$_{PV}$	32	0.062/8	0.0198+0.0483i	4.1256
AHM$_{WPP2}$	27.3	0.062/13	0.0215+0.0487i	2.1288

TABLE I.   PARAMETERS OF THE AGGREGATED HARMONIC MODELS OF WIND POWER AND PHOTOVOLTAIC PLANTS (AHM$_{WPP}$ AND AHM$_{PV}$)

B. Case Study 1: Wind Power Plant

The WPP is connected to a transmission system by a 240-MVA substation of 230/34.5 kV and 60 Hz. Fig. 4 shows a single-line diagram of the detailed model of the WPP (DM$_{WPP}$) connected to the power grid. The details of WT generators (G11-G26), transformers (T11-T26), impedances, control gains, and other electric parameters are available in [24].

A power quality analyzer Fluke 1748 was installed at the medium-voltage side of transformer T11. The harmonic currents produced by generator G11 were measured at the rated power according to the IEC 61400-21 standard. The most significant harmonic amplitudes were 0.012%, 0.027%, 0.122%, and 0.11% for the 2nd, 3rd, 5th, and 7th orders, respectively. Harmonic currents are expressed as a percentage of the rated current considering base values of 28.2 MW and 34.5 kV. The voltage unbalance factor and total harmonic voltage distortion (THD$_v$) were 0.34% and 0.31%, respectively. The three phase-to-ground voltages of the 230-kV power grid ($v_{ga,b,c}$) were v_{ga}=132.79∠0° kV, v_{gb}=132.79∠239.75° kV, and v_{gc}=131.98∠120° kV. The background distortion consisted of a harmonic voltage V_3 = 0.31% for the 3rd order.
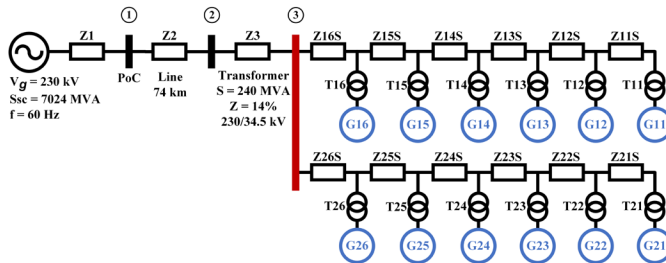
Figure 4.   Single-line electric circuit representing the detailed model of the wind power plant (DM$_{WPP}$) connected to a transmission system.

Fig. 5a presents the current profile produced by the DM$_{WPP}$ and AHM$_{WPP}$ at the rated power. These currents are injected into the bus 3 shown in Fig. 4. Fig. 5b exhibits the discrepancy signal of the current waveform generated by the AHM$_{WPP}$, when it is compared to the reference current of the DM$_{WPP}$.
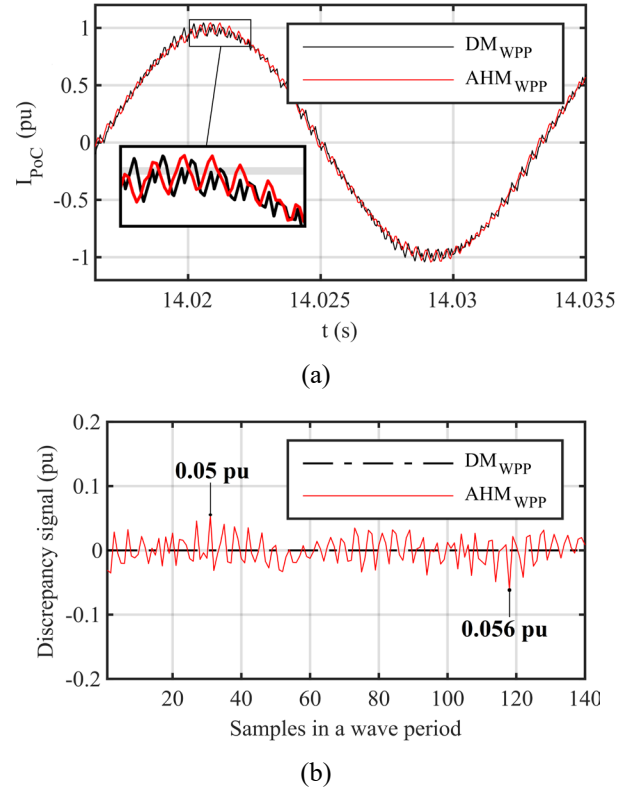

(a)

(b)

Figure 5.   (a) Current waveforms produced by the DM$_{WPP}$ and AHM$_{WPP}$; (b) discrepancy signal obtained comparing the AHM$_{WPP}$ and DM$_{WPP}$ curves.

Based on Fig. 5a, we verify that the AHM$_{WPP}$ current follows the DM$_{WPP}$ curve and reproduces fast-scale oscillations generated by the switching devices. Fig. 5b shows that the maximum discrepancy between the waveforms was 0.056 pu. These results demonstrate that the AHM$_{WPP}$ produces current profiles with minor discrepancies. This occurs because the AHM$_{WPP}$ uses commutation functions to reproduce the switching behavior from the DM$_{WPP}$.

Fig. 6 presents the DM$_{WPP}$ and AHM$_{WPP}$ frequency responses of the impedance magnitude and angle measured at bus 3 of Fig. 4. Based on Fig. 6, we verify that DM$_{WPP}$ produces impedance peaks at 500 Hz and 2120 Hz with magnitudes of 91.5 and 88.5 pu, respectively. The AHM$_{WPP}$ generates impedance peaks in 499 Hz and 2118 Hz with magnitudes of 70.5 and 96 pu, respectively. The angles from both models vary from 90° to -90° with approximately the same behavior.

These results indicate that the AHM$_{WPP}$ provides an adequate frequency response corresponding to its equivalent impedance. In other words, the impedance of the AHM$_{WPP}$ (in Table I) accurately represent the resonance of the DM$_{WPP}$.

(a)

(b)

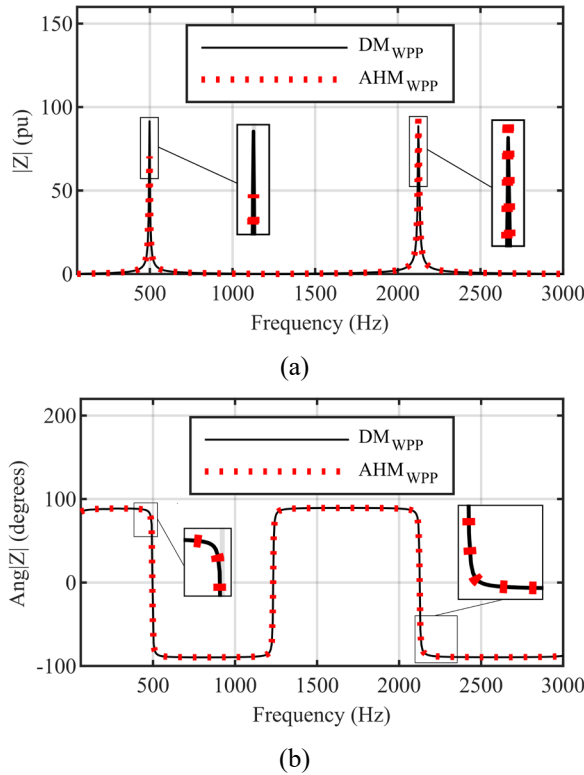Figure 6. (a) Magnitude and (b) angle responses of the WPP produced by the DM_{WPP} and AHM_{WPP}, respectively.

Finally, we consider the measured harmonic currents produced by generator G11 and use the second summation law of IEC (13) to obtain the IEC-based spectrum of the entire plant.

$$I_h = \sqrt[\alpha]{\sum_k^{q_{total}} I_{h,k}^\alpha} \qquad \begin{matrix} \alpha = 1 \text{ for } h < 5; \\ \alpha = 1.4 \text{ for } 5 \le h \le 10; \\ \alpha = 2 \text{ for } h > 10 \end{matrix} \qquad (13)$$

where $I_{h,k}$ represents the hth order contribution from generator k, and q_{total} denotes the number of generators in the plant.

Fig. 7 presents the IEC-based and simulated harmonic spectra of the DM_{WPP} and AHM_{WPP} on bus 3 of Fig. 4 at the rated power. The simulated spectra were obtained via fast Fourier transform (FFT) method. Fig. 7 shows that the measured IEC-based spectrum exhibits amplitudes of 0.33%, 0.72%, and 0.63% for the 3rd, 5th, and 7th orders, respectively. The IEC-based spectrum presents a total harmonic current distortion (THD_i) of 1.17%. The AHM_{WPP} produces amplitudes of 0.26%, 0.62%, and 0.61% for the 3rd, 5th, and 7th orders, respectively. The THD_i generated by the AHM_{WPP} was 0.97%. The maximum discrepancy was 0.2% when comparing the measured and the simulated spectra. These results indicate that the AHM_{WPP} can estimate the harmonic currents in WPP with discrepancies lower than 0.2%.
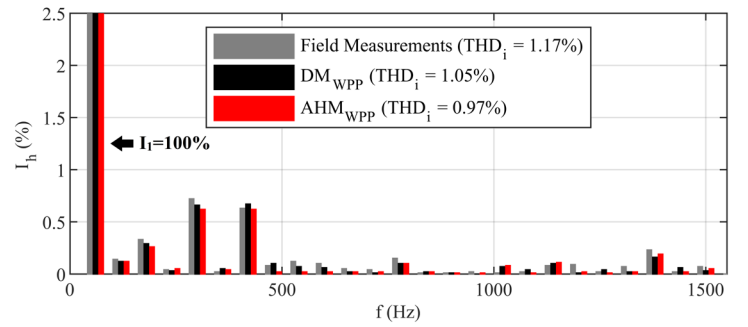

Figure 7. IEC-based spectrum and simulated harmonic spectra of the WPP considering the DM_{WPP} and AHM_{WPP}, respectively.

C. Case Study 2: Photovoltaic Plant

The PV power plant is connected to a transmission system by a 178-MVA substation of 138/34.5 kV and 60 Hz. Fig. 8 shows the single-line diagram of the detailed model of this PV system (DM_{PV}), which includes inverters (In11-In24), transformers (T11-T24), impedances, harmonic filters, and capacitor banks (CBs). A complete list of the system parameters is available in [24].
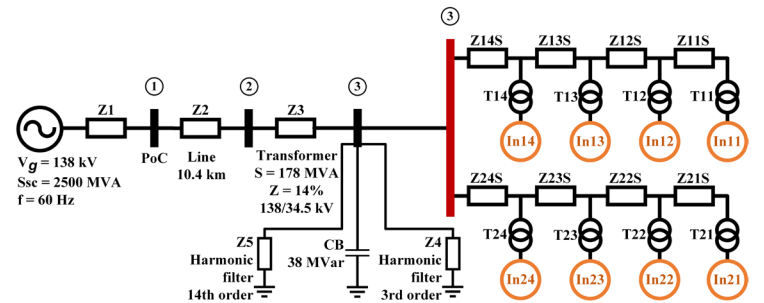

Figure 8. Single-line electric circuit representing the detailed model of the photovoltaic plant (DM_{PV}) connected to a transmission system.

A power quality analyzer ION 7650 was installed at the medium-voltage side of transformer T21. The harmonic currents produced by inverter In21 were measured at the rated power, according to the IEC 61400-21 standard. The most significant harmonic amplitudes were 0.023%, 0.03%, 0.02%, 0.144%, and 0.12% for the 2nd, 3rd, 4th, 5th, and 7th orders, respectively. Harmonic currents are expressed as percentages of the rated current considering base values of 34.5 kV and 32 MW. The voltage unbalance factor and THD_v recorded by the analyzer were 0.45% and 1.02%, respectively. The three phase-to-ground voltages of the 138-kV power grid ($v_{ga,b,c}$) were v_{ga} =79.67∠0° kV, v_{gb} =79.67∠239.49° kV, and v_{gc} =79.27∠120° kV. The background distortion consisted of harmonic voltages of $V_3 = 0.64\%$ and $V_5 = 0.80\%$ for the 3rd and 5th orders, respectively.

Fig. 9a exposes the current profile produced by the DM_{PV} and AHM_{PV} at the rated power. These currents are injected into the bus 3 shown in Fig. 8. Fig. 9b presents the discrepancy signal of the current waveform generated by the AHM_{PV}, when it is compared to the reference current of the

DM_{PV}. Based on Fig. 9a, we identify that the AHM_{PV} reproduces the fast-scale oscillations from the switching process of the DM_{PV}. Fig. 9b shows that the maximum discrepancy between the waveforms was 0.065 pu. These results indicate that the AHM_{PV} produces current profiles with minor discrepancies because it uses commutation functions to reproduce the switching behavior from the DM_{PV}.
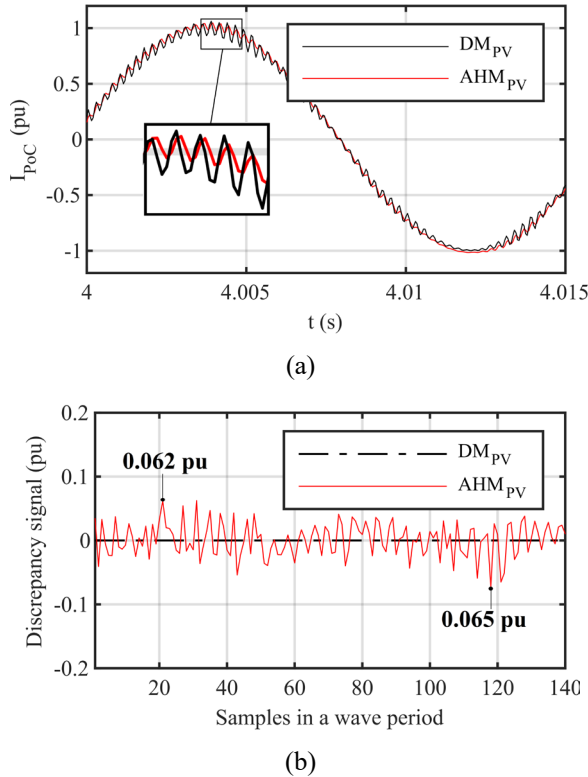

(a)

(b)

Figure 9. (a) Current waveforms produced by the DM_{PV} and AHM_{PV}; (b) discrepancy signal obtained comparing the AHM_{PV} and DM_{PV} curves.

Fig. 10 exposes the DM_{PV} and AHM_{PV} frequency responses of the impedance magnitude and angle measured at bus 3 of Fig. 8. Based on Fig. 10, we identify that DM_{PV} generates impedance peaks at 678 Hz and 1884 Hz with magnitudes of 86 and 77 pu, respectively. The AHM_{PV} displays impedance peaks at 677 Hz and 1886 Hz with magnitudes of 75 and 65 pu, respectively. The angles from both models vary from 90° to -90° with similar behavior.

These results indicate that the AHM_{PV} provides an adequate frequency response corresponding to its equivalent impedance. In other words, the impedance of the AHM_{PV} (in Table I) accurately represent the resonance of the DM_{PV}.
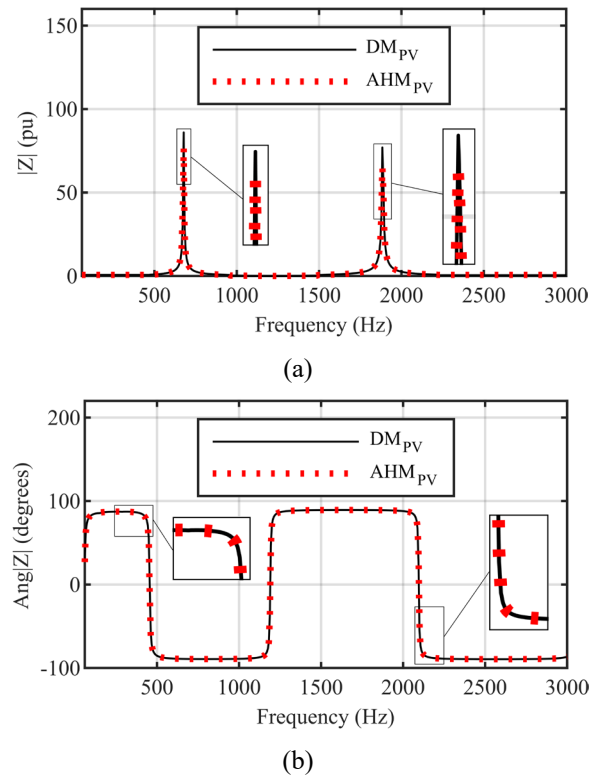

(a)

(b)

Figure 10. (a) Magnitude and (b) angle responses of the PV plant produced by the DM_{PV} and AHM_{PV}, respectively.

Fig. 11 displays the IEC-based spectrum (13) and harmonic spectra of the DM_{PV} and AHM_{PV} on bus 3 of Fig. 8 at the rated power.
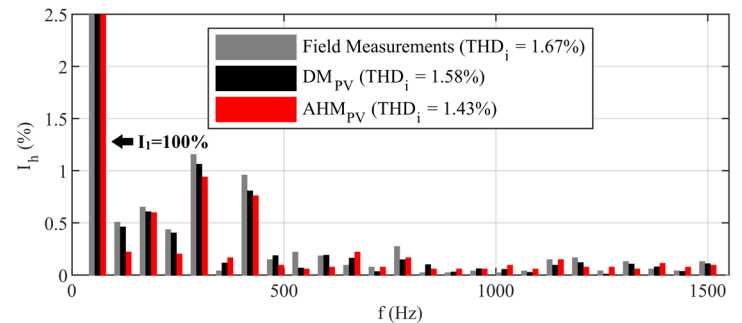

Figure 11. IEC-based spectrum and simulated harmonic spectra of the PV plant considering the DM_{PV} and AHM_{PV}, respectively.

Based on Fig. 11, we see that the IEC-based spectrum consists of amplitudes of 0.5%, 0.65%, 0.43%, 1.15%, and 0.95% for the 2nd, 3rd, 4th, 5th, and 7th orders, respectively. The AHM_{PV} exhibits amplitudes of 0.22%, 0.6%, 0.2%, 0.94%, and 0.76% for the 2nd, 3rd, 4th, 5th, and 7th orders, respectively. The maximum discrepancy observed for even orders was 0.32% and that for odd orders was 0.19%. The THD_i discrepancy was 0.24% when comparing the measured and simulated spectra. These analyses demonstrate that the

AHM$_{PV}$ can estimate the harmonic currents in PV plants with discrepancies lower than 0.4%.

D. Case Study 3: Validation using Field Measurements

This plant has thirteen 2.1-MW WTs connected to a transmission system by a 150-MVA substation of 230/34.5 kV and 60 Hz. Fig. 12 shows a single-line diagram of the WPP and the resulting AHM$_{WPP2}$.
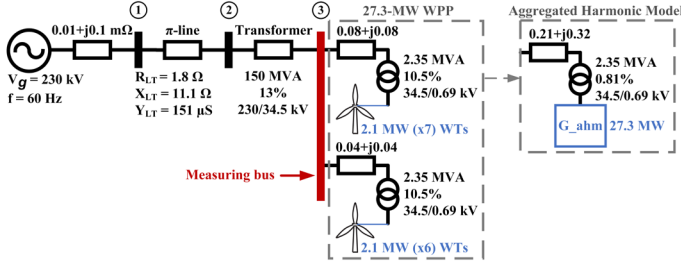

Figure 12. Single-line electric circuit representing the 27.3-MW WPP used in the validation process and the resulting AHM$_{WPP2}$.

A Fluke 435-II was installed at bus 3 according to the IEC 61400-21 standard. We measured the aggregated harmonic currents produced by the WPP and compared them with the AHM results for injections of 60% and 100% of the rated power. The voltage unbalance factor and THD$_v$ recorded by the analyzer were 1.2% and 0.63%, respectively. Table III presents the measured and simulated spectra up to the 13th order.

	Injection of 60%			Injection of 100%		
	Field	AHM$_{WPP2}$	Discrepancy	Field	AHM$_{WPP2}$	Discrepancy
Orders	(%)	(%)	(%)	(%)	(%)	(%)
1st	100	100	0	100	100	0
2nd	3.49	2.82	0.67	1.86	1.35	**0.51**
3rd	3.44	3.15	0.29	2.44	2.22	0.22
4th	2.41	1.73	**0.68**	1.55	1.17	0.38
5th	1.00	1.21	-0.21	0.75	1.08	-0.33
6th	1.20	0.74	0.46	0.67	0.42	0.25
7th	0.39	0.66	-0.27	0.32	0.44	-0.12
8th	0.78	0.24	0.54	0.62	0.15	0.47
9th	0.74	0.54	0.20	0.34	0.33	0.01
10th	0.36	0.13	0.23	0.29	0.14	0.15
11th	0.44	0.39	0.05	0.19	0.22	-0.03
12th	0.13	0.02	0.11	0.16	0.04	0.12
13th	0.21	0.24	-0.03	0.31	0.19	0.12
THD$_i$ (%)	**5.89**	**5.11**	**0.78**	**3.76**	**3.09**	**0.67**

TABLE II.   MEASURED AND SIMULATED SPECTRA OF THE 27.3-MW WPP.

For an injection of 60% of the rated power, the maximum discrepancy was 0.68% for the 4th (240 Hz) order. For an injection of 100% of the rated power, the maximum discrepancy was 0.51% for the 2nd (120 Hz) order. When considering the THD$_i$, a maximum discrepancy of 0.78% was observed at different power levels. These results indicate that the spectrum provided by the AHM$_{WPP2}$ is an adequate approximation of the measured spectrum with discrepancies lower than 0.8%.

E. Computational Efforts

The simulations were conducted on a Microsoft Windows 10 operating system with a 3.3 GHz Intel(R) Core (TM) i97900X CPU and 64 GB of RAM. The responses of the DMs

and AHMs were observed for 15 s. The time step of the simulation is 5 μs. Table III lists the computation times and discrepancies of the DM$_{WPP}$, DM$_{PV}$, AHM$_{WPP}$, AHM$_{PV}$, and AHM$_{WPP2}$.

	DM$_{WPP}$	DM$_{PV}$	AHM$_{WPP}$	AHM$_{PV}$	AHM$_{WPP2}$
Time (s)	3427	2985	24.5	23.8	25.1
Maximum discrepancy (%)	-	-	0.2	0.32	0.78

TABLE III.   COMPUTATION TIMES AND DISCREPANCIES OF THE DM$_{WPP}$, DM$_{PV}$, AHM$_{WPP}$, AHM$_{PV}$, AND AHM$_{WPP2}$.

Based on Table III, we verify that the AHM$_{WPP}$ reduces the computation time of the DM$_{WPP}$ by 99.3%, whereas the AHM$_{PV}$ reduced the computation time of the DM$_{PV}$ by 99.2%. The maximum discrepancy observed during the tests was 0.78% in the case study 3. These results demonstrate that the proposed AHM performs simulations with a low computational burden and produces accurate results.

IV. CONCLUSIONS

This paper proposed a novel time-domain model based on a single machine topology for harmonic assessment in WPPs or PV plants. The AHM considered dead time and switching effects in its simplification, providing a computationally efficient solution for system-level harmonic studies. Detailed WPP and PV plant models were utilized as references during the simulations, and field measurements from another WPP validated the harmonic estimation capability of the AHM.

The results demonstrate that the AHM can generate fast accurate current profiles, frequency responses, and harmonic current spectra. Across all case studies evaluated in this work, a maximum discrepancy of 0.78% was observed. These findings underscore the effectiveness of the AHM as a tool for system operators and decision-makers in the planning and operating sectors, enabling them to analyze the penetration impacts of RESs on large-scale power systems and identify potential resonance conditions and harmonic issues.

Future research should explore additional scenarios and validate the AHM under diverse operating conditions to enhance its applicability and robustness. Overall, employing the AHM allows system agents to recommend strategies for mitigating harmonic emissions from power plants and ensuring the stability and reliability of the grid.

REFERENCES

[1] S. Impram, S. Varbak Nese, and B. Oral, "Challenges of renewable energy penetration on power system flexibility: A survey," *Energy Strateg. Rev.*, vol. 31, p. 100539, Apr. 2020.

[2] Q. Zhang, L. Zhou, M. Mao, B. Xie, and C. Zheng, "Power quality and stability analysis of largescale grid-connected photovoltaic system

considering non-linear effects," *IET Power Electron.*, vol. 11, no. 11, pp. 1–9, Sep. 2018.

[3] W. Li, P. Chao, X. Liang, J. Ma, D. Xu, and X. Jin, "A Practical Equivalent Method for DFIG Wind Farms," *IEEE Trans. Sustain. Energy*, vol. 9, no. 2, pp. 610–620, Apr. 2018.

[4] J. Brochu, C. Larose, and R. Gagnon, "Validation of single- and multiple-machine equivalents for modeling wind power plants," *IEEE Trans. Energy Convers.*, vol. 26, no. 2, pp. 532–541, Jun. 2011.

[5] P. H. F. Moraes, A. Reis, A. L. F. Filho, "Novel time-domain average model for harmonic current prediction in photovoltaic and wind power units," *Intern. Trans. on Elect. Energy Syst.*, vol. 31, no. 12, pp. e13253, Nov. 2021.

[6] G. Todeschini, S. Balasubramaniam, P. Igic, "Time-domain modeling of a distribution system to predict harmonic interaction between PV converters," *IEEE Trans. on Sustain. Energy*, vol. 10, no. 3, pp. 1450-1458, Feb. 2019.

[7] J. Peralta, H. Saad, S. Dennetière, J. Mahseredjian, S. Nguefeu, "Detailed and averaged models for a 401-level MMC–HVDC system," *IEEE Trans. on Power Deliv.*, vol. 27, no. 3, pp. 1501-1508, 2012.

[8] X. Zha, S. Liao, M. Huang, Z. Yang, and J. Sun, "Dynamic Aggregation Modeling of Grid-Connected Inverters Using Hamilton's-Action-Based Coherent Equivalence," *IEEE Trans. Ind. Electron.*, vol. 66, no. 8, pp. 6437–6448, Aug. 2019.

[9] W. Li, P. Chao, X. Liang, D. Xu, and X. Jin, "An Improved Single-Machine Equivalent Method of Wind Power Plants by Calibrating Power Recovery Behaviors," *IEEE Trans. Power Syst.*, vol. 33, no. 4, pp. 4371–4381, Jul. 2018.

[10] P. Wang, Z. Zhang, Q. Huang, N. Wang, X. Zhang, and W. J. Lee, "Improved wind farm aggregated modeling method for large-scale power system stability studies," *IEEE Trans. Power Syst.*, vol. 33, no. 6, pp. 6332–6342, Nov. 2018.

[11] J. Zou, C. Peng, H. Xu, and Y. Yan, "A Fuzzy Clustering Algorithm-Based Dynamic Equivalent Modeling Method for Wind Farm with DFIG," *IEEE Trans. Energy Convers.*, vol. 30, no. 4, pp. 1329– 1337, Dec. 2015.

[12] Y. Zhou, L. Zhao, I. B. M. Matsuo, and W. J. Lee, "A Dynamic Weighted Aggregation Equivalent Modeling Approach for the DFIG Wind Farm Considering the Weibull Distribution for Fault Analysis," *IEEE Trans. Ind. Appl.*, vol. 55, no. 6, pp. 5514–5523, Dec. 2019.

[13] N. Wang et al., "A novel method for wind farm equivalence based on multi-objective optimization," in *Proc. 2018 IEEE PES Asia-Pacific Power and Energy Engineering Conference*, pp. 353–358, Oct. 2018.

[14] J. Martínez-Turégano, S. Añó-Villalba, S. Bernal-Perez, and R. Blasco-Gimenez, "Aggregation of type-4 large wind farms based on admittance model order reduction," *Energies*, vol. 12, no. 9, pp. 1– 21, May 2019.

[15] H. Wang, C. Buchhagen, and J. Sun, "Methods to aggregate turbine and network impedance for wind farm resonance analysis," *IET Renew. Power Gener*, vol. 14, no. 8, pp. 1304–1311, Dec. 2019.

[16] W. Cao, K. Liu, S. Wang, H. Kang, D. Fan, and J. Zhao, "Harmonic stability analysis for multi-parallel inverter-based grid-connected renewable power system using global admittance," *Energies*, vol. 12, no. 14, Jul. 2019.

[17] B. Badrzadeh and M. Gupta, "Power System Harmonic Analysis in Wind Power Plants - Part I: Study Methodology and Techniques," in *Proc. 2012 IEEE Industry Applications Society Annual Meeting*, p. 27, Oct. 2012.

[18] X. Wang and F. Blaabjerg, "Harmonic Stability in Power Electronic-Based Power Systems: Concept, Modeling, and Analysis," *IEEE Trans. Smart Grid*, vol. 10, no. 3, pp. 2858–2870, May 2019.

[19] P. Pourbeik et al., "Generic Dynamic Models for Modeling Wind Power Plants and Other Renewable Technologies in Large-Scale Power System Studies," *IEEE Trans. Energy Convers.*, vol. 32, no. 3, pp. 1108–1116, Sep. 2017.

[20] J. Kwon, X. Wang, F. Blaabjerg, C. L. Bak, V. S. Sularea, and C. Busca, "Harmonic Interaction Analysis in a Grid-Connected Converter Using Harmonic State-Space (HSS) Modeling," *IEEE Trans. Power Electron.*, vol. 32, no. 9, pp. 6823–6835, Sep. 2017.

[21] J. Garcia, P. Garcia, F. G. Capponi, and G. De Donato, "Analysis, modeling, and control of half-bridge current-source converter for energy management of supercapacitor modules in traction applications," *Energies*, vol. 11, no. 9, pp. 1–22, Aug. 2018.

[22] A. Guha and G. Narayanan, "Average modelling of a voltage source inverter with dead-time in a synchronous reference frame," in *Proc. 2013 IEEE Innovative Smart Grid Technologies-Asia*, pp. 1–6, Nov. 2013.

[23] D. G. Holmes and T. A. Lipo, "Modulation of three-phase voltage source inverters," in *Pulse Width Modulation for Power Converters*, New York: John Wiley & Sons, 2003, pp. 215-259.

[24] P. H. F. Moraes, PSCC 2022 - Data Sharing, Figshare. 2021 [Online]. Available: http://doi.org/10.6084/m9.figshare.16649443.